Z. Angew. Math. Phys. (2025) 76:124

https://doi.org/10.1007/s00033-025-02517-7

Zeitschrift für angewandte Mathematik und Physik ZAMP

Hyperfoams: Energy dissipation and shock wave formation

Vladimir Bratov and Sergey V. Kuznetsov

Abstract. It has been found that highly porous organic foams (hyperfoams) modeled by the Blatz–Ko and Hill hyperelastic potentials may exhibit mechanical energy loss caused by the formation and propagation of strain discontinuities arising when a portion of a faster wave pulse overtakes a slower one. This observation opens up a possibility for creating a new type of shock absorbers containing no viscous or dry friction elements. For example, the considered Blatz–Ko-type hyperelastic potential is a good material behavior model for moderately stiff polyurethane (PU) foams both at large compression and at large extension strains. The analysis utilizes a combined method consisting of the explicit time integration technique coupled with the finite element method for spatial discretization.

Mathematics Subject Classification. 74J40.

Keywords. Hyperfoam, Shock absorber, Shock wave front, Blatz–Ko potential, Acoustic wave, Energy dissipation.

1. Introduction

1.1. Overview

Currently, various rigid highly porous organic foam materials (hyperfoams) are widely used as shock absorbers due to their ability to attenuate mechanical wave energy [1]; also see Fig. 1a. It was assumed that this attenuation takes place because of two main mechanisms (i) scattering of acoustic waves by pores [2] and (ii) viscoelastic properties of the skeleton material [3]. Meanwhile, theoretical studies based on the two-scale asymptotic analysis testify that waves with wavelengths that are several orders of magnitude larger as compared to the typical pore dimension can hardly be scattered by small pores [4,5]. Similarly, the considered viscoelastic effects can make a significant impact on multiple loading cycles (e.g., during vibration) [6,7], but are not able to provide sufficient attenuation for propagating bulk waves, especially single short-duration pulses at sufficiently small distances from the excitation source [8,9]. Note that a stochastic hyperfoam structure can also be observed in aerogels [10] (Fig. 1b).

The majority of non-porous stitched polymers exhibiting almost no compressibility in a large range of principal stretches, which are actually eigenvalues of the Cauchy–Green strain tensors, are modeled by the non-compressible versions of the Ogden potential [12,13], Mooney–Rivlin potential [14–18], Yeoh potential [19–21], or Arruda–Boyce potential [22–25]. However, the considered highly porous polymers demonstrate large compressibility with a complicated but monotonic variation of Cauchy stress vs. strain [26–30].

To model highly porous elastic materials, Hill [31] proposed the following potential

$$W(\lambda_1, \lambda_2, \lambda_3) = \sum_{m \in M} \frac{C_m}{|m|} \left(\sum_{k=1}^{3} \lambda_k^m - 3 + \frac{1}{|n|} \left(J^{-mn} - 1 \right) \right), \tag{1.1}$$

Published online: 26 May 2025

Birkhäuser

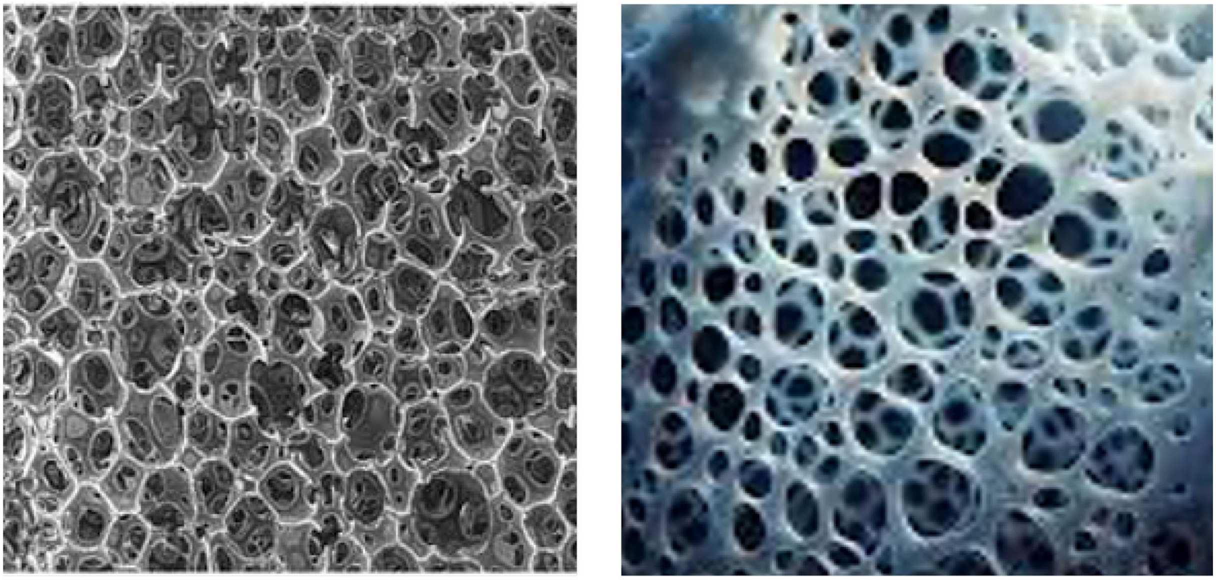

(A) Polyurethane (PU) hyperfoam [11] (B) Aerogel [10]

FIG. 1. Microstructure of typical hyperfoams

where λ_k, $k = 1, 2, 3$ are the eigenvalues (principal stretches) of the strain gradient $\mathbf{F}$, C_m are the experimentally defined coefficients, M is a finite set of real numbers, and

$$J \equiv \det(\mathbf{F}) = \lambda_1\lambda_2\lambda_3. \tag{1.2}$$

With potential 1.1, the principal components of the Cauchy stress tensor become

$$\sigma_i = \lambda_i^{-1} \sum_{m\in M} C_m \left(\lambda_i^m - J^{-nm}\right). \tag{1.3}$$

Note that according to [31] neither of the exponents m or n need to be positive and integer. Considering uniaxial tension–compression with conditions

$$\lambda_1 = \lambda; \qquad \sigma_2 = \sigma_3 = 0 \tag{1.4}$$

and taking into account Eqs.1.3, Storåkers [32] constructed expressions for the eigenvalues λ_k $k = 2, 3$

$$\lambda_k = \lambda^{-\frac{n}{2n+1}}, \qquad k = 2, 3. \tag{1.5}$$

Blatz & Ko [33], analyzing hyperfoams made of polyurethanes, revealed that the general potential 1.1 can be reduced to the following one-parametric form with $m = -2$ and $n = 2^{-1}$, which yields

$$W(\lambda_1, \lambda_2, \lambda_3) = \frac{\mu}{2}\left(\sum_{k=1}^{3} \lambda_k^{-2} + 2J - 5\right). \tag{1.6}$$

Equation 1.5 for the Blatz–Ko potential 1.6 yields

$$\lambda_k = \lambda^{-\frac{1}{4}}, \qquad k = 2, 3. \tag{1.7}$$

The apparent non-smooth variation of the potential at $\lambda \to 1 \pm 0$ visible in Fig. 2a disappears when moving from the semi-logarithmic scale to the Cartesian scale in Fig. 2b. The plots in Fig. 2 demonstrate the nonlinear behavior of the elastic potential over the whole range of uniaxial stretches $\lambda \in [0.2;\ 1.2]$, ensuring nonlinearity in the stress–stretch relation [27]. It should also be noted that the considered

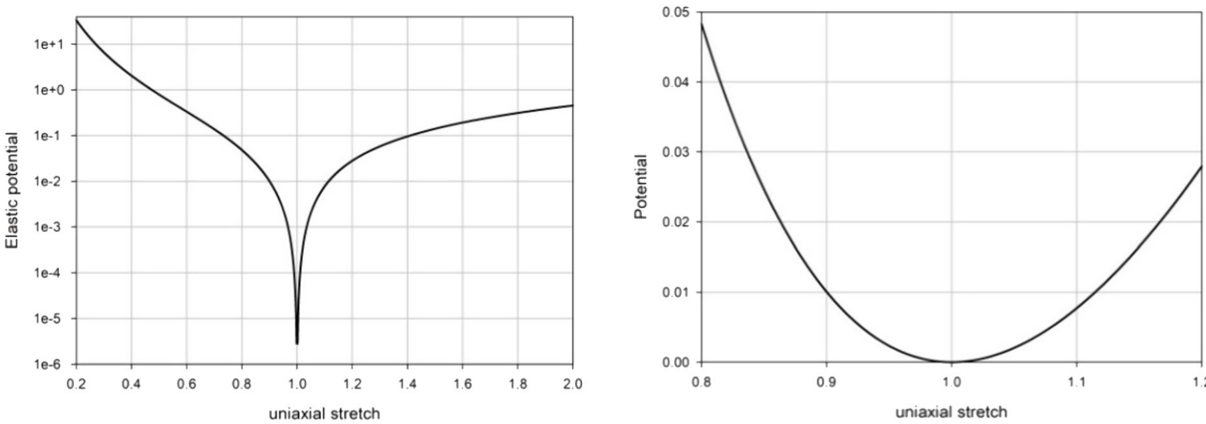

(A) Semi-logarithmic scales (B) Cartesian scales in the vicinity of $\lambda = 1$

FIG. 2. The Blatz–Ko potential for hyperfoam under uniaxial compression–tension

potential 1.6 along with a more general potential 1.1 is quite often used for modeling different polymeric materials with high porosity [34–37]. Karp and Durban [38] reported a comprehensive analysis of dynamic spectral response of prestressed plates with material behavior given by Blatz–Ko potential.

1.2. Problem statement

Herein, uniaxial wave propagation in a hyperfoam rod modeled by the Blatz–Ko potential 1.6 is analyzed, revealing, apparently for the first time, (i) the formation and propagation of (strong) shock wave fronts associated with discontinuities in the strain field; (ii) the attenuation of displacement magnitudes with distance from the excitation source; therefore, (iii) the attenuation of both kinetic and strain energy; and (iv) the simultaneous release of thermal energy. These observations may indicate that the most probable mechanism for the attenuation of waves in a hyperfoam material can be associated with the formation and propagation of shock wave fronts and not the previously assumed viscous properties of the material [39, 40], or scattering by micropores [3]. Thus, it is demonstrated that mechanical energy dissipation can be achieved in a purely hyperelastic system without viscous or dry friction properties.

The current analysis is based on solving nonlinear hyperbolic equation for a traveling stress wave in a hyperfoam material modeled by the Blatz–Ko potential 1.6. The solution for the considered hyperbolic equation is constructed by the finite element (FE) method for spatial discretization coupled with an explicit energy-preserving Lax–Wendroff numerical scheme for time integration.

2. Governing equations

2.1. Cauchy stress, tangent modulus, and rod velocity

The Cauchy principal stress [41] for potential 1.6 and conditions 1.7 takes the form

$$\sigma_1(\lambda) \equiv \partial_\lambda W(\lambda) = \mu \left(\lambda^{\frac{5}{2}} - 1\right) \lambda^{-3}, \tag{2.1}$$

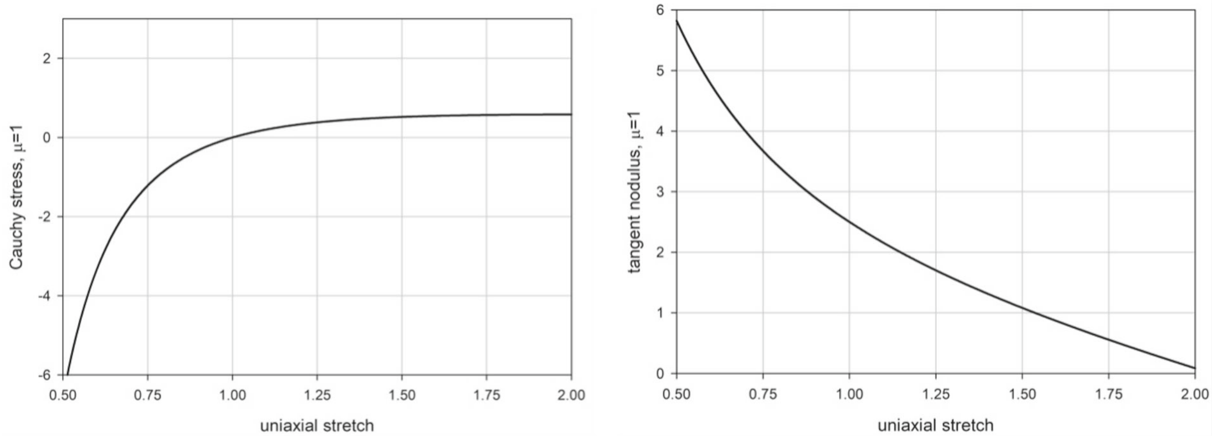

(A) Cauchy stress vs. stretch.

(B) Tangent elastic modulus vs. stretch.

FIG. 3. The Blatz–Ko potential

Hereafter, the subscript at the principal stress will be omitted. Differentiating this principal stress with λ yields the tangent elastic modulus

$$E(\lambda) \equiv \partial_\lambda \sigma(\lambda) = \frac{1}{2}\mu\left(6 - \lambda^{\frac{5}{2}}\right)\lambda^{-4}. \tag{2.2}$$

The material density is defined as [41]

$$\rho(\lambda) \equiv \rho_0 J^{-1} = \rho_0 \lambda^{-\frac{1}{2}}, \tag{2.3}$$

where ρ_0 is the material density at the natural state, assumed to be at $\lambda = 1$. Now, following [42–44] and accounting Eqs.2.2, 2.3 introduce the rod velocity, which is the propagating velocity of an arbitrary stress pulse in a one-dimensional rod

$$c(\lambda) \equiv \sqrt{\frac{E(\lambda)}{\rho(\lambda)}} = \sqrt{\frac{\mu}{2\rho_0}\left(6 - \lambda^{\frac{5}{2}}\right)\lambda^{-\frac{3}{2}}}. \tag{2.4}$$

Remark. The obtained expression 2.2 for tangent elastic modulus is valid for

$$\lambda < 6^{\frac{2}{5}} \approx 2.048, \tag{2.5}$$

from where the Blatz–Ko potential 1.6 becomes non-convex (loses ellipticity). This fact was mentioned and studied in several works [32,45–50]. Herein, it is assumed that the tensile stretches do not exceed the estimate 2.5. The plots in Fig. 3 show the variation of Cauchy stress and tangent modulus with stretch, varying in the range $\lambda \in [0.5; 2.0]$.

2.2. Equation of motion

The equation of motion for the considered one-dimensional case can be written in the form [41]

$$\partial_x \sigma(\lambda) = \rho(\lambda)\partial^2_{tt} u(x,t), \tag{2.6}$$

where $u(x,t)$ is the displacement field, related to the principal stretch λ of the corresponding diagonal deformation gradient $\mathbf{F}$

$$\mathbf{F} = \partial_x u(x,t)\mathbf{n} \otimes \mathbf{n} + \mathbf{I} \tag{2.7}$$

FIG. 4. Semi-infinite rod

by the following relation [13]

$$\lambda = 1 + \partial_x u(x,t). \tag{2.8}$$

In Eq. 2.7 **I** is the unit 3×3-matrix (tensor), and **n** is the unit vector directed along the axis of the rod.

Now, in view of Eqs.2.1, 2.2, and 2.8, the desired equation of motion takes the form of a nonlinear hyperbolic equation

$$F\left(\partial_x u(x,t)\right)\partial_{xx}^2 u(x,t) = \partial_{tt}^2 u(x,t), \tag{2.9}$$

where

$$F\left(\partial_x u(x,t)\right) \equiv \frac{\mu}{2\rho_0}\left(6 - (1+\partial_x u(x,t))^{\frac{5}{2}}\right)(1+\partial_x u(x,t))^{-\frac{3}{2}}. \tag{2.10}$$

2.3. Boundary and initial conditions

Consider a semi-infinite rod with a triangle loading applied at the left edge:

$$p(t) = p_0 \begin{cases} 0, & t < 0 \\ t, & 0 < t < t_0 \\ 2t_0 - t, & t_0 < t < 2t_0 \\ 0, & 2t_0 < t \end{cases}, \tag{2.11}$$

where $2t_0$ is the pulse duration and p_0 is a dimensional constant, specifying the intensity of the applied force load (Fig. 4).

The Sommerfeld attenuation condition [51,52] is imposed at the right end ($x \to \infty$):

$$u(x,t)|_{x\to\infty} = 0; \qquad \partial_x u(x,t)|_{x\to\infty} = 0. \tag{2.12}$$

The initial conditions correspond to the state of rest:

$$u(x,t)|_{t=0} = 0 \qquad \partial_t u(x,t)|_{t=0} = 0. \tag{2.13}$$

2.4. Equations of energy balance

The equation of energy balance can be written in the form [41]

$$\int_0^t P(\tau)d\tau = E_k + E_s + Q, \tag{2.14}$$

where Q is the heat release, defined by the release of specific thermal energy, as

$$Q \equiv \int_0^t \int_0^\infty q(x,\tau)dxd\tau. \tag{2.15}$$

In Eq. 2.14 E_k and E_s are the kinetic and strain energy, respectively

$$E_k = \frac{1}{2}\int_0^\infty \rho(\lambda(x,t))(\partial_t u(x,t))^2 dx \qquad E_s = \frac{1}{2}\int_0^\infty W\left(\lambda(x,t)\right)dx, \tag{2.16}$$

and $P(\tau)$ is the power of external force $f(\tau)$

$$P(\tau) = f(\tau)\partial_\tau u(0,\tau). \tag{2.17}$$

When shock wave fronts associated with discontinuities in strain appear, Eq. 2.14 needs to be supplemented with a balance equation at the shock wave front [53,54]

$$\rho_0 V\left[W\right] + \frac{1}{2}\rho_0 V\left[c^2\right] = -\left[\sigma c\right] + \left[Q\right], \tag{2.18}$$

where the square brackets denote the jump at the discontinuity and V is the velocity of the moving shock wave front. Equation 2.18 allows us to define the shock wave velocity:

$$V = \frac{[Q] - [\sigma c]}{\rho_0\left[W\right] + \frac{1}{2}\rho_0\left[c^2\right]}. \tag{2.19}$$

Note that according to [41]

$$c_{\min} < V < c_{\max}, \tag{2.20}$$

where $c_{\min},\ c_{\max}$ are the limiting values of particle velocities at both sides of the shock wave fronts.

2.5. FE formulation

The governing equations are solved by applying FE method for spatial discretization and the FD method in the time-domain coupled with an explicit Lax–Wendroff energy conservation numerical scheme [51,55]. To achieve a conditionally stable numerical algorithm, the Courant–Friedrichs–Lewi (CFL) condition is imposed on the time increment Δt, which for the considered problem reads as [56,57]

$$\Delta t < \Delta t_{CFL} \equiv \frac{\Delta x}{\max\limits_{\lambda} c(\lambda)}, \tag{2.21}$$

where Δt_{CFL} is the CFL time increment, Δt is the time increment, Δx is the spatial increment (mesh size), and $c(\lambda)$ is the rod velocity, defined by Eq.2.4; the principal stretch λ satisfies the convexity condition

$$\partial^2_{\lambda\lambda} W(\lambda) = \frac{1}{2}\mu\left(6 - \lambda^{\frac{5}{2}}\right)\lambda^{-4} > 0, \tag{2.22}$$

and, thus, λ should satisfy condition 2.5. In the current analysis, a two-step predictor–corrector form of the Lax–Wendroff scheme is used [51]

$$\begin{aligned} u\left(x_{j+1/2}; t_{n+1/2}\right) = \tfrac{1}{2}\left(u\left(x_{j+1}; t_n\right) + u\left(x_j; t_n\right)\right) - \\ \tfrac{\Delta t}{2\Delta x}\left(F\left(u\left(x_{j+1}; t_n\right)\right) - F\left(u\left(x_j; t_n\right)\right)\right) \end{aligned}, \tag{2.23}$$

where x_j is a spatial node and F is the nonlinear function, defined by Eq.2.10.

The explicit dynamics finite element commercial software ANSYS LS-DYNA [58] was utilized to solve the problem numerically. There was no possibility to utilize simplest two-node linear elements with Blatz–Ko material model in LS-DYNA ® software, so more complicated 2D elements with rotational symmetry were used to simulate wave propagating in the rod (Fig. 4), with a load given by Eq. 2.11. To perform mesh convergence analysis, total number of elements was varied in the range $7K \leq N \leq 22K$. The mesh convergence analysis reveals almost identical displacement and stress fields for $N \geq 10K$; hence, $N \approx 10K$ was chosen for the further computational analysis. Instead of imposing the Sommerfeld attenuation condition 2.12 at $x \to \infty$, the points of observation were chosen in such a way to ensure the absence of reflected waves from the right end of the rod. In the current model, the load at the left end of the rod was defined by Eq. 2.11 with $t_0 = 30\ \mu s$ and $p_0 = 150N$.

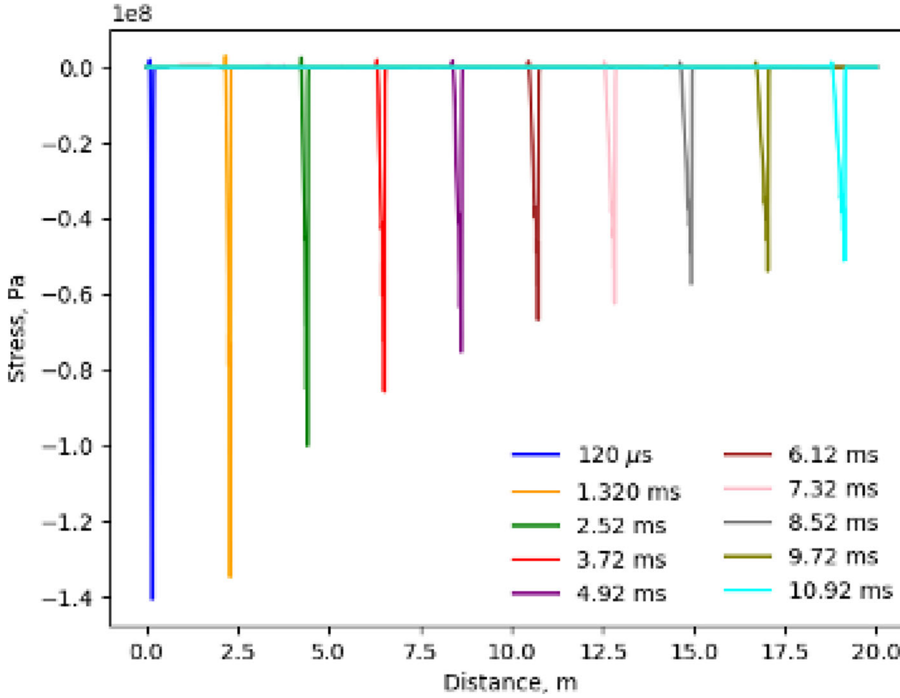

FIG. 5. Compressive load pulse traveling along the rod. Different colors are referred to different times

3. Numerical analysis

The force loading shown in Fig. 4 and defined by Eq. 2.11 reveals that the applied delta-like pulse generates the initially triangle pulse propagating with variable velocity dependent upon ε by Eq. 2.4. Since the speed of propagation and material density are highly dependent upon strain ε, as plots in Fig. 3 show, some parts of the pulse may travel faster than others. These overtakes result in (i) an overlap of the slower moving parts of the leading wave front by the faster moving parts contained inside the pulse; this phenomenon causes the formation of multiple shock wave fronts; (ii) spreading out the initially narrow triangle and its distortion; and (iii) decrease in mechanical energy due the formation and propagation of shock wave fronts, at which the mechanical energy dissipation occurs [53]. All these phenomena are observed at propagating wave pulse in the considered Blatz–Ko rod (see Fig. 5), where the variation of the principal component of the Cauchy stress tensor versus time is plotted. Herein, the Cauchy stress tensor is defined as [41]

$$\sigma = J^{-1}\frac{\partial W}{\partial \mathbf{F}} \cdot \mathbf{F}, \tag{3.1}$$

yielding the desired principal component for σ, and the Lagrangian finite strain tensor

$$\mathbf{E} = \frac{1}{2}\left(\mathbf{B} - \mathbf{I}\right). \tag{3.2}$$

The typical stress pulses at the origin ($t = 120\,\mu s$) and somewhere in the middle of the rod ($t = 8.52\,ms$), where the shock wave front is formed, are given in Fig. 6.

The variation of the pulse stress amplitude versus distance is plotted in Fig. 7, revealing a substantial decrease in the stress amplitudes with distance.

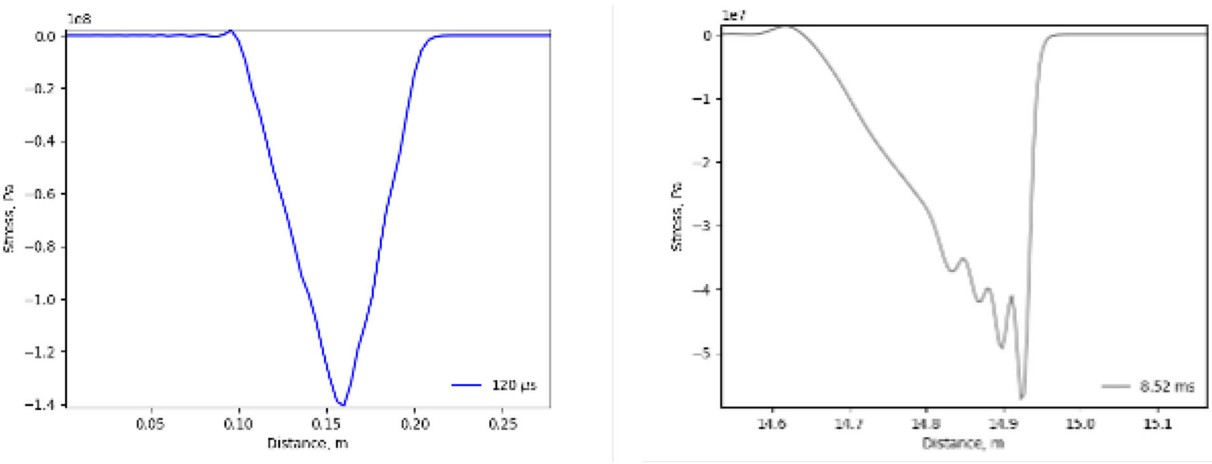

(A) (B)

Fig. 6. The compressive wave shape for: a) initial time and b) time when the shock wave front is formed

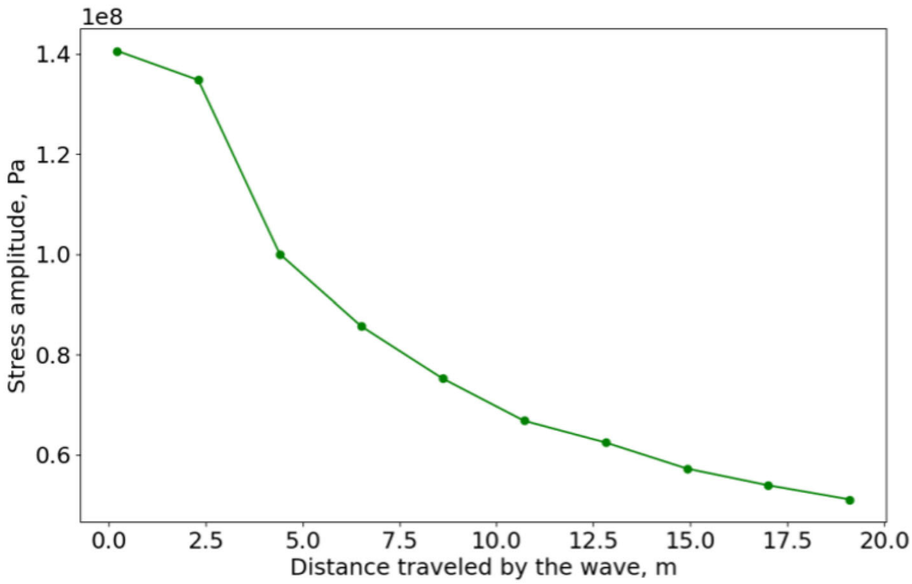

Fig. 7. The amplitude of the stress pulse as a function of distance traveled by the pulse along the rod

It has also been observed that both kinetic and strain energy decrease with time and distance from the left end of the rod, while heat is released in the expense of the losses in mechanical energy.

4. Concluding remarks

Analyzing excitation of the delta-like acoustic waves propagating in a semi-infinite rod modeled by the Blatz–Ko hyperelastic potential, which describes the stress–strain relations of various foams, including polymer hyperfoams [9] and aerogels [10, 30, 59], revealed that the elastic tangent modulus (Fig. 3a) varies monotonically with strain in the whole range of admissible values of the principal stretch 2.5, ensuring the convexity of the considered potential. Regarding the propagation of the delta-like pulses along the rod, it has been observed that the Cauchy stress attenuates with the distance (Figs. 5 and 7), caused by the formation and propagation of the shock wave fronts, which appear at the head fronts of the pulses (Fig. 6). Moreover, the performed analysis also revealed that both kinetic and strain energy dissipate resulting in the significant thermal energy release. Cohen and Durban [60] proposed a theoretical framework for the propagation of longitudinal shock waves in elastoplastic solids, utilizing an analogy to the piston-driven shock tube model commonly employed in fluid dynamics. This formulation was subsequently extended to account for steady shock waves in porous elastoplastic media [61]. The findings from these studies elucidate an additional dissipation mechanism for shock wave energy, namely plastic deformation within the solid matrix. Thus, apparently for the first time, the loss of mechanical energy is observed at the propagation of acoustic waves in a purely mechanical system, modeled by the Blatz–Ko potential, ensuring a continuous and smooth variation of mechanical properties. This phenomenon reveals a possibility for the mechanical wave attenuation due to the formation and propagation of the shock wave fronts.

Declarations

Conflict of interest The authors declare that they have no conflict of interest.

References

[1] Hakan, U., Ipek, B.: Dynamic characterization and modeling of rubber shock absorbers: A comprehensive case study. J. Low Freq. Noise Vibr. Active Control **37**(3), 146134841772595 (2018)
[2] Das, G., Chakraborty, R.: Effect of porosity on wave scattering by a vertical porous barrier over a rectangular trench. J. Marine Sci. Appl. **23**, 85–100 (2024)
[3] Vriend, N.M., Kren, A.P.: Determination of the viscoelastic properties of elastomeric materials by the dynamic indentation method. Polym. Test. **23**, 369–375 (2004)
[4] Bensoussan, A., Lions, J.L.: Asymptotic Analysis for Periodic Structures. North Holland, Amsterdam (1978)
[5] Allaire, G.: Homogenization and two-scale convergence. SIAM J. Math. Anal. **23**(6), 1482–1518 (1992)
[6] Brown, R.: Physical Testing of Rubber. Springer, New York (2006)
[7] Goldstein, R.V., et al.: The modified Cam-Clay (MCC) model: cyclic kinematic deviatoric loading. Arch. Appl. Mech. **86**(12), 2021–2031 (2016)
[8] Carcione, J.M., Kosloff, D., Kosloff, R.: Wave propagation simulation in a linear viscoelastic medium. Geophys. J. Int. **95**, 597–611 (1988)
[9] Berjamin, H., Destrade, M., Saccomandi, G.: Singular travelling waves in soft viscoelastic solids of rate type. Eur. J. Mech. A **103**, 105144 (2024)
[10] Lyu, Sh., et al.: Effect of high temperature on compression property and deformation recovery of ceramic fiber reinforced silica aerogel composites. Sci. China Technol. Sci. **60**(11), 1681–1691 (2017)
[11] Bashirzadeh, R., Gharehbaghi, A.: An investigation on reactivity, mechanical and fire properties of PU flexible foam. J. Cellular Plast. **46**(2), 129–158 (2010)
[12] Ogden, R.W.: Waves in isotropic elastic materials of Hadamard, Green, or harmonic type. J. Mech. Phys. Solids **18**(2), 149–163 (1970)

[13] Ogden, R.W.: Nonlinear Elastic Deformations. Dover Publications, New York (1984)
[14] Murphy, J.G.: Strain energy functions for a Poisson power law function in simple tension of compressible hyperelastic materials. J. Elast. **60**, 151–164 (2000)
[15] Boulanger, P., Hayes, M.A.: Finite amplitude waves in Mooney-Rivlin and Hadamard materials. In: Topics in Finite Elasticity, eds. Hayes, M.A., Saccomandi, G., Springer, Wien (2001)
[16] Treloar, L.R.G.: The Physics of Rubber Elasticity. Oxford University Press, Oxford (2005)
[17] Hamza, M., Hassan, A.: Hyperelastic constitutive modeling of rubber and rubber-like materials under finite strain. Eng. Tech. J. **28**(13), 2560–2575 (2010)
[18] Chen, J., Garcia, E.S., Zimmerman, S.C.: Intramolecularly cross-linked polymers: From structure to function with applications as artificial antibodies and artificial enzymes. Acc. Chem. Res. **53**(6), 1244–1256 (2020)
[19] Yeoh, O.H.: Some forms of the strain energy function for rubber. Rubber Chem. Technol. **66**(5), 754–771 (1993)
[20] Gajewski, M., Szczerba, R., Jemioło, S.: Modelling of elastomeric bearings with application of Yeoh hyperelastic material model. Procedia Eng. **111**, 220–227 (2015)
[21] Pence, T.J., Gou, K.: On compressible versions of the incompressible neo-Hookean material. Math. Mech. Solids **20**(2), 157–182 (2015)
[22] Arruda, E.M., Boyce, M.C.: A three-dimensional model for the large stretch behavior of rubber elastic materials. J. Mech. Phys. Solids **41**(2), 389–412 (1993)
[23] Boyce, M.C.: Direct comparison of the Gent and the Arruda-Boyce constitutive models for rubber elasticity. Rubber Chem. Technol. **69**, 781–785 (1996)
[24] Boyce, M.C., Arruda, E.M.: Constitutive models of rubber elasticity: A review. Rubber Chem. Technol. **73**(3), 504–523 (2000)
[25] Bergstrom, J.S., Boyce, M.C.: Deformation of elastomeric networks: Relation between molecular level deformation and classical statistical mechanics models of rubber elasticity. Macromolecules **34**(3), 614–626 (2001)
[26] Beatty, M.F.: Topics in finite elasticity: hyperelasticity of rubber, elastomers, and biological tissues-with examples. Appl. Mech. Rev. **40**(12), 1699–1734 (1987)
[27] Parmeneter, K.E., Milstein, F.: Mechanical properties of silica aerogels. J. Non-Crystalline Solids **223**(3), 179–189 (1998)
[28] Landauer, A., et al.: Experimental characterization and hyperelastic constitutive modeling of open-cell elastomeric foams. J. Mech. Phys. Solids **133**, 103701 (2019)
[29] Bresler, F.H., Muller, J.H., Venter, G.: Investigating an inverse Finite Element approach for characterising soft materials. R&D J. **37**, 80–88 (2021)
[30] Patil, S.P., et al.: Mechanical modeling and simulation of aerogels: A review. Ceram. Int. **47**, 2981–2998 (2021)
[31] Hill, R.: Aspects of invariance in solid mechanics. Adv. Appl. Mech. **18**, 1–72 (1978)
[32] Storåkers, B.: On material representation and constitutive branching in finite compressible elasticity. J. Mech. Phys. Solids **34**(2), 125–145 (1986)
[33] Blatz, P.D., Ko, W.L.: Application of finite elasticity to the deformation of rubbery materials. Trans. Soc. Rheol. **6**, 223–251 (1962)
[34] Kakavas, P.A.: Influence of the cavitation on the stress-strain fields of compressible Blatz-Ko materials at finite deformation. Int. J. Solids Struct. **39**, 783–795 (2002)
[35] Peyraut, F.: Loading restrictions for the Blatz-Ko hyperelastic model-application to a finite element analysis. Int. J. Non-Linear Mech. **39**, 969–976 (2004)
[36] Hadoush, A.: Effect of Poisson's ratio on internally balanced Blatz-Ko material model. Acta Mech. Sinica **39**, 422350 (2023)
[37] Bozkurt, M.O., Tagarielli, V.L.: A data-driven constitutive model for porous elastomers at large strains. Extr. Mech. Lett. **70**, 102170 (2024)
[38] Karp, B., Durban, D.: Evanescent and propagating waves in prestretched hyperelastic plates. Int. J. Solids Struct. **42**, 1613–1647 (2005)
[39] Li, S., et al.: Explicit/implicit multi-time step co-simulation in unbounded medium with Rayleigh damping and application for wave barrier. Eur. J. Environ. Civil Eng. **24**(14), 2400–2421 (2020)
[40] Li, S., et al.: Benchmark for three-dimensional explicit asynchronous absorbing layers for ground wave propagation and wave barriers. Comput. Geotech. **131**, 103808 (2021)
[41] Truesdell, C., Noll, W.: The Non-Linear Field Theories of Mechanics, 3rd edn. Springer, Berlin (2004)
[42] Kolsky, H.: Stress waves in solids. J. Sound Vibr. **1**, 88–110 (1964)
[43] Ilyashenko, A.V., et al.: Theoretical aspects of applying Lamb waves in nondestructive testing of anisotropic media. Russ. J. Nondestruct. Test. **53**, 243–259 (2017)
[44] Ilyashenko, A.V., et al.: Pochhammer-Chree waves: polarization of the axially symmetric modes. Arch. Appl. Mech. **88**, 1385–1394 (2018)
[45] Knowles, J.K., Sternberg, E.: On the singularity induced by certain mixed boundary conditions in linearized and nonlinear elastostatics. Int. J. Solids Struct. **11**, 1173–1201 (1975)

[46] Knowles, J.K., Sternberg, E.: On the failure of ellipticity and the emergence of discontinuous deformation gradients in plane finite elastostatics. J. Elasticity **8**, 329–379 (1978)
[47] Thompson, J.M.T., Shorrock, P.A.: Bifurcational instability of an atomic lattice. J. Mech. Phys. Solids **23**, 21–37 (1975)
[48] Kuznetsov, S.V.: "Forbidden" planes for Rayleigh waves. Quart. Appl. Math. **60**(1), 87–97 (2002)
[49] Kuznetsov, S.V.: Love waves in stratified monoclinic media. Quart. Appl. Math. **62**(4), 749–766 (2004)
[50] Li, S., et al.: Hybrid asynchronous absorbing layers based on Kosloff damping for seismic wave propagation in unbounded domains. Comput. Geotech. **109**, 69–81 (2019)
[51] Belytschko, T., Liu, W.K., Moran, B.: Nonlinear Finite Elements for Continua and Structures. Wiley, N.Y. (2000)
[52] Terentjeva, E.O., et al.: Planar internal Lamb problem: Waves in the epicentral zone of a vertical power source. Acoust. Phys. **61**, 356–367 (2015)
[53] Truesdell, C.: General and exact theory of waves in finite elastic strain. Arch. Ration. Mech. Anal. **8**, 263–296 (1961)
[54] Bland, D.R.: On shock structure in a solid. J. Inst. Math. Appl. **1**, 56–75 (1965)
[55] Lax, P.D., Wendroff, B.: Difference schemes for hyperbolic equations with high order of accuracy. Commun. Pure Appl. Math. **17**, 381–398 (1964)
[56] Scovazzi, G., Song, T., Zeng, X.: A velocity/stress mixed stabilized nodal finite element for elastodynamics: Analysis and computations with strongly and weakly enforced boundary conditions. Comput. Methods Appl. Mech. Eng. **325**(1), 532–576 (2017)
[57] Winnicki, I., Jasinski, J., Pietrek, S.: New approach to the Lax-Wendroff modified differential equation for linear and nonlinear advection. Numer. Meth. Part. Differ. Eq. **35**, 2275–2304 (2019)
[58] ANSYS Inc.: ANSYS LS-DYNA simulation software. (2024). https://lsdyna.ansys.com
[59] Guild, M.D., et al.: Aerogel as a soft acoustic metamaterial for airborne sound. Phys. Rev. Appl. **5**, 034012 (2016)
[60] Cohen, T., Durban, D.: Longitudinal shock waves in solids: the piston shock analogue. Proc. R. Soc. A. **470**, 20130061 (2014)
[61] Cohen, T., Durban, D.: Steady shock waves in porous plastic solids. Int. J. Solids Struct. **71**, 70–78 (2015)

Vladimir Bratov
Edinburgh Napier University
Edinburgh
UK
e-mail: v.bratov@napier.ac.uk

Sergey V. Kuznetsov
Moscow State University of Civil Engineering
Moscow
Russia
e-mail: kuzn-sergey@yandex.ru

(Received: March 20, 2025; revised: April 25, 2025; accepted: May 12, 2025)